Volume 13
Number 36
28 September 2025
Pages 18525–19066

Journal of Materials Chemistry C

Materials for optical, magnetic and electronic devices

rsc.li/materials-c

ISSN 2050-7526

ROYAL SOCIETY OF **CHEMISTRY**

PAPER
Ziang Cui *et al.*
A printable liquid metal–montmorillonite ink for high-resolution stretchable bioelectronics

Journal of
Materials Chemistry C

ROYAL SOCIETY
OF CHEMISTRY

PAPER

View Article Online
View Journal | View Issue

Check for updates

Cite this: *J. Mater. Chem. C*, 2025, **13**, 18638

A printable liquid metal–montmorillonite ink for high-resolution stretchable bioelectronics

Ziang Cui,[a] Yiqing Zhang,[a] Siyuan Chen,[b] Xingming Wen,[a] Yining Zhao,[c] Yitao Ma,[b] Qihang Yan,[c] Zixiong Wu,[d] Yuxi He,[b] Guohui Wang,[a] Ziyuan Tang,[c] Chenxi Xiao,[c] You Yu,[aef] Jianrui Li*[g] and Ze Xiong*[aef]

Gallium-based liquid metals (LMs) are emerging as leading materials for flexible and stretchable bioelectronics due to their exceptional electrical conductivity and mechanical malleability. However, the inherently high surface tension of LMs hinders both their printability and adhesion to substrates, creating significant barriers to scalable, high-resolution patterning. Here, we present an effective strategy to overcome these challenges by formulating a printable liquid metal–montmorillonite (LM–MMT) composite ink. This LM–MMT ink demonstrates markedly improved rheological properties, facilitating reliable direct printing of high-resolution, stretchable, and highly conductive patterns on a broad range of substrates. Strain sensors fabricated from the LM–MMT ink exhibit high sensitivity, minimal hysteresis, and exceptional fatigue resistance across more than 100 cycles of deformation. These sensors enable accurate real-time monitoring of both gross human joint movements and subtle motion signals such as swallowing and neck rotation. Furthermore, we demonstrate that multi-channel strain sensing arrays based on LM–MMT ink enable real-time hand gesture recognition and robotic hand control, establishing a robust and seamless human–machine interface. This work introduces a scalable, cost-effective additive manufacturing strategy for LMs, openning new avenues for wearable sensing, continuous health monitoring, and next-generation intelligent interactive bioelectronics.

Received 11th June 2025,
Accepted 13th August 2025

DOI: 10.1039/d5tc02256h

rsc.li/materials-c

1. Introduction

The advancement of electronic devices capable of seamlessly conforming to curved and highly deformable surfaces, such as human joints, has become pivotal for next-generation health monitoring and human–machine interaction systems.[1] Traditional rigid electronics, constrained by their lack of stretchability and flexibility, are fundamentally unsuited for integration with dynamic biological tissues.[2] In response to these challenges, flexible and stretchable bioelectronics have emerged as transformative platforms, enabling intimate and robust interfacing with the human body.[3–5] Among various candidates for stretchable conductors, gallium-based liquid metals—such as gallium (Ga), eutectic gallium–indium alloy (EGaIn), and gallium–indium–tin alloy (GaInSn)—have garnered immense attention owing to their excellent metallic conductivity and intrinsic stretchability. These materials exhibit outstanding biocompatibility and safety, characterized by negligible toxicity and low vapor pressure at room temperature,[6–9] positioning them as ideal materials for wearable and implantable bioelectronics.[10,11] To realize the full potential of these materials, various fabrication techniques, such as stamp printing,[12] stencil printing,[13,14] inkjet printing,[15] and direct writing,[16] have been developed for patterning liquid metals into functional architectures. Among these, direct ink writing (DIW) is an additive manufacturing technique that enables precise, site-specific material deposition. This approach minimizes material waste and facilitates the fabrication of complex geometries with improved pattern resolution.[17–21] However, the inherently high surface tension and superior fluidity of gallium-based liquid metals pose significant challenges during processing, promoting aggregation and the spontaneous formation of spherical droplets with minimized surface energy.[22,23] Compounding the issue, many commonly used flexible substrates (*e.g.*, paper, textiles) are "supermetallophobic" or "oxide-phobic", exhibiting poor

---

[a] *School of Biomedical Engineering, ShanghaiTech University, Shanghai 201210, P. R. China. E-mail: xiongze@shanghaitech.edu.cn*
[b] *School of Physical Science and Technology, ShanghaiTech University, Shanghai 201210, P. R. China*
[c] *School of Information Science and Technology, ShanghaiTech University, Shanghai 201210, P. R. China*
[d] *Department of Biomedical Engineering, National University of Singapore, Singapore 117583, Singapore*
[e] *State Key Laboratory of Advanced Medical Materials and Devices, ShanghaiTech University, Shanghai 201210, P. R. China*
[f] *Shanghai Clinical Research and Trial Center, Shanghai 201210, P. R. China*
[g] *Department of Plastic Surgery, Zhongshan Hospital, Fudan University, Shanghai 200032, P. R. China. E-mail: jianrui@zs-hospital.sh.cn*

wetting and weak adhesion toward liquid metals.[24] These combined factors impede the scalable fabrication of high-resolution, reliable liquid metal patterns across diverse substrates.

To overcome the challenges associated with surface tension and substrate adhesion, a promising approach involves dispersing liquid metal micro- or nanodroplets within polymer matrices to create printable inks. Such inks are amenable to screen printing and direct writing, enabling efficient deposition on a range of substrates.[25] However, conductivity in these systems is often compromised: micro/nanodroplets are encapsulated by insulating gallium oxide layers or polymers, yielding initially non-conductive patterns.[26] Conductive activation typically requires post-printing mechanical pressure to rupture the encapsulating shells and coalesce droplets,[27,28] which constrains both patterning resolution and electrical stability. An alternative and increasingly explored solution is the formulation of composite liquid metal inks through the admixture of solid particles, including Fe,[29] Ni,[14,16,30] Cu,[31,32] Ag,[33] and carbon nanotube,[34] to yield hybrid pastes with improved printability, while maintaining high conductivity without the need for post-processing activation. Importantly, these composite inks also often display improved substrate adhesion, expanding the versatility of liquid metals for flexible and stretchable electronics. Nevertheless, previous efforts have frequently relied on metallic fillers due to their propensity to form intermetallic bonds with gallium, thereby facilitating wettability and mechanical integrity of the resulting composites.[35] Unfortunately, such processes typically demand the use of acidic or basic media during mixing, increasing fabrication complexity and overall costs.[36]

To address these persistent limitations, we report here a facile and cost-effective strategy for producing direct-ink-writing (DIW)-compatible composite liquid metal (LM) inks by mechanically blending montmorillonite (MMT) micro powder with gallium-based liquid metal. MMT, a naturally abundant and inexpensive clay, offers high chemical stability and ease of processing as a filler. Utilizing a planetary mixing and degassing protocol, we obtain a homogeneous LM–MMT ink exhibiting tunable flowability, favorable pseudoplasticity, and exceptional electrical conductivity, eliminating the need for any external conductive activation. The resultant shear-thinning ink permits reliable, high-resolution DIW patterning on a variety of substrates, rendering it highly suitable for the fabrication of flexible and stretchable bioelectronics. Strain sensors fabricated using the LM–MMT ink display high sensitivity, low hysteresis, and excellent durability through repeated deformation cycles, effectively capturing both subtle motion signals and gross joint movements in real time. Furthermore, multi-channel LM–MMT sensing array provides a robust platform for gesture recognition and remote robotic control, establishing seamless human–machine interfaces. Therefore, this work not only unlocks new material opportunities for liquid metal-based electronics but also introduces a scalable, cost-effective pathway for additive manufacturing in wearable sensing, health monitoring, and intelligent interactive bioelectronics.

Ze Xiong

Ze Xiong is an assistant professor at ShanghaiTech University's School of Biomedical Engineering in Shanghai, China. He received his PhD from The University of Hong Kong under the supervision of Prof. Jinyao Tang, and subsequently worked as a research fellow at the National University of Singapore, collaborating with Prof. Chwee Teck Lim, Prof. Benjamin C. K. Tee, and Prof. John S. Ho. His research focuses on developing wireless and flexible bioelectronics to advance clinical and personalized healthcare through digital intelligence. He has received the MINE Young Scientist Award, the Emerging Investigator of China Award, and recognition as an iCANX Young Scientist Award Finalist. In 2025, he was awarded the Young Scientists Fund B (formerly the Excellent Young Scientists Fund).

2. Results and discussion

2.1 Design of LM–MMT ink

The intrinsically high surface tension of gallium-based liquid metals poses substantial challenges for DIW and the formation of continuous, high-fidelity printed tracks, thereby limiting their widespread application in stretchable bioelectronics. To address these limitations, functional additives are required to modulate surface tension and printability. In this work, montmorillonite powder was mechanically blended into the liquid metal matrix, resulting in a composite LM–MMT ink with significantly enhanced printability and substrate wettability (Fig. 1a). Utilizing pressure-driven direct ink writing technology, the LM–MMT ink enables reliable deposition of continuous, conductive patterns onto a wide variety of substrates, faithfully reproducing predesigned geometries. In contrast, pure liquid metal, owing to its high surface tension, tends to form droplets upon extrusion, thereby compromising the integrity and resolution of printed structures (Movie S1). Compared to other commonly used fillers in liquid metal inks, the inclusion of MMT achieves an optimal balance between high conductivity and cost-effectiveness, while also providing excellent performance in terms of printing resolution and substrate compatibility (Fig. 1b and Table S1).[29–32,37–44]

The process from pure liquid metal to LM–MMT ink is illustrated in Fig. 1c: pure liquid metal displays a metallic sheen and exists as a shapeless, highly fluid entity at room temperature, while the initial addition of MMT powder sits atop the liquid metal due to surface tension effects. After thorough mechanical mixing, the blend transforms into a homogeneous, silver-white paste with decreased flowability, yet maintains adequate fluidic properties for printing.

The optimized LM–MMT ink enables direct ink writing of diverse, complex curvilinear patterns (Fig. 1d and e). The printed traces possess narrow linewidths and high resolution while preserving structural integrity and accommodating

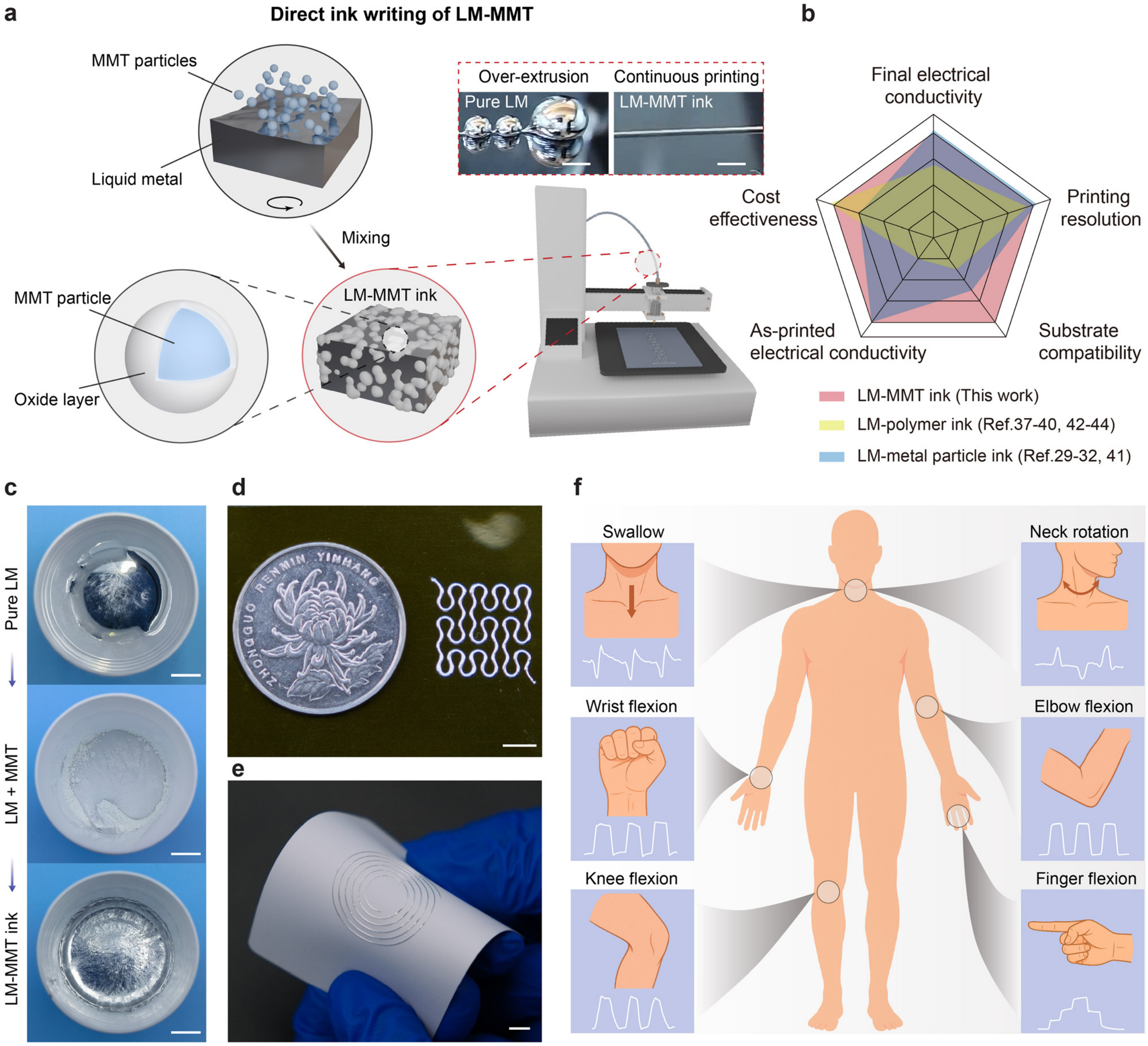

Fig. 1 Design, preparation, and applications of LM–MMT ink for stretchable bioelectronics. (a) Schematic of the preparation and printing of LM–MMT inks. Scale bars: 5 mm. (b) Comparative performance metrics between the LM–MMT ink and previously reported inks in literature. (c) Photos depicting the stepwise preparation of LM–MMT ink: pure liquid metal (top), liquid metal with montmorillonite added (middle), and fully mixed LM–MMT ink (bottom). Scale bars: 10 mm. (d) High-resolution serpentine pattern printed with LM–MMT ink. Scale bar: 5 mm. (e) Printed LM–MMT coil with excellent substrate adhesion and flexibility. Scale bar: 5 mm. (f) Human motion signals detected by LM–MMT-based bioelectronic sensors.

deformations such as bending or twisting of the substrate (Movie S2). Importantly, the LM–MMT ink retains excellent electrical conductivity without the need for any additional thermal or mechanical activation post-printing. Collectively, these attributes establish the LM–MMT ink as a promising material for scalable, rapid, and high-resolution fabrication of bioelectronic devices. To demonstrate the versatility of the LM–MMT ink for health monitoring and motion detection, stretchable bioelectronic sensors were tailored to varying anatomical locations (Fig. 1f), enabling detection of both gross (*e.g.*, wrist, elbow, knee, and finger flexion/extension) and subtle physiological motions (*e.g.*, swallowing and neck rotation).

2.2. Preparation and characterizations of LM–MMT Ink

Preparation of the LM–MMT ink entailed adding predetermined mass fractions of MMT powder (2.5%, 5%, 7.5%, and 10% relative to liquid metal) to EGaIn in a planetary mixer. The mixture was subjected to thorough blending and degassing until a homogeneous slurry was obtained (Fig. 2a). MMT is a naturally abundant, non-toxic clay consisting of layered silicate structures. Each layer contains two tetrahedral silica sheets sandwiching a central octahedral alumina sheet, with partial Al^{3+}/Mg^{2+} substitution in the octahedral sites.[45,46] MMT appears as white, flake-like powder. Scanning electron microscopy (SEM) and energy-dispersive spectroscopy (EDS) confirmed that MMT

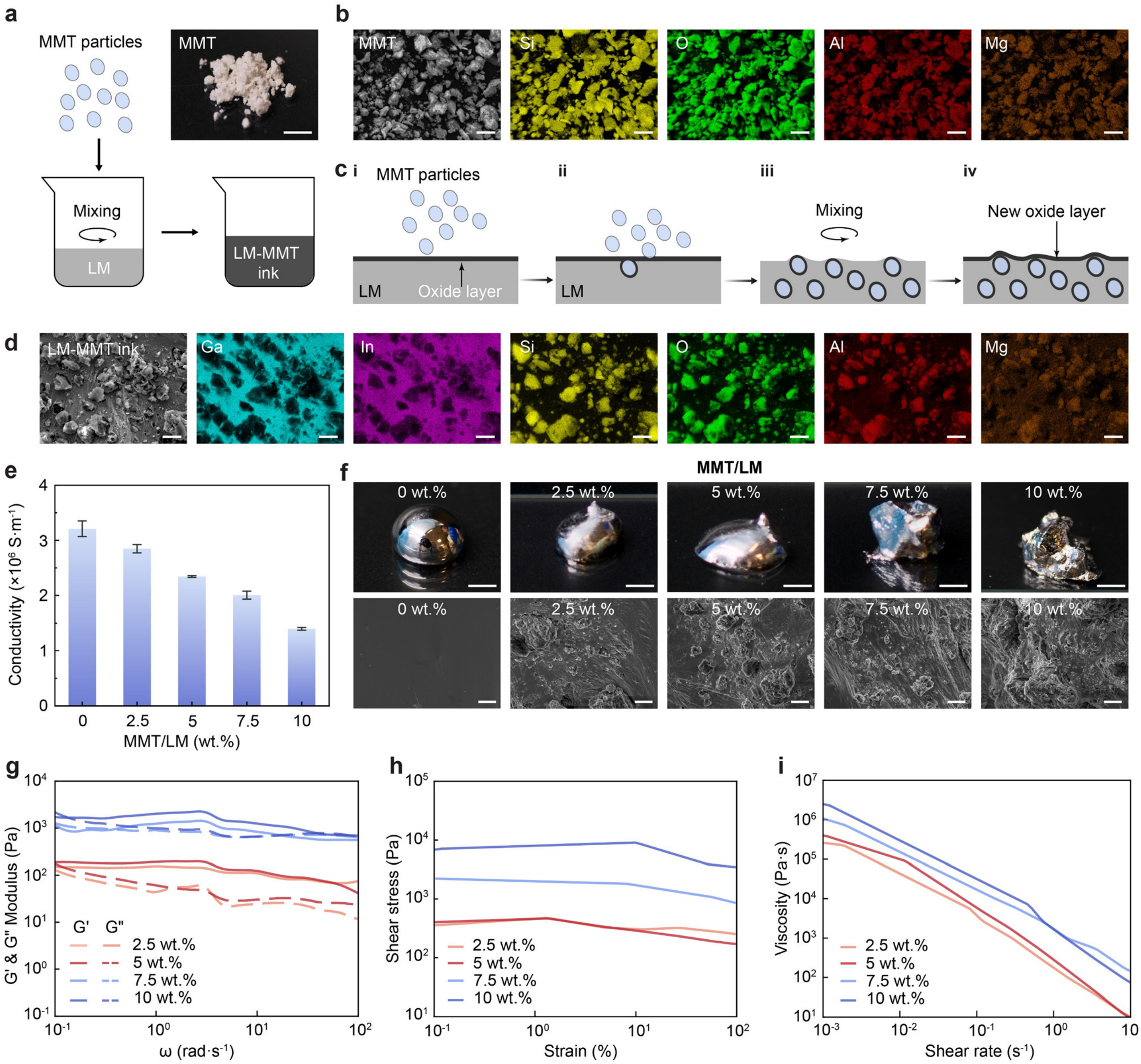

Fig. 2 Structural and rheological characterization of LM–MMT inks. (a) Schematic of the LM–MMT ink preparation process, accompanied by an optical image of the MMT powders. Scale bar: 2 mm. (b) SEM image and corresponding element mapping (EDS) of MMT powders. Scale bars: 10 μm. (c) Illustration depicting the mixing mechanism by which MMT powders are uniformly integrated into the liquid metal. (d) SEM image and EDS mapping of the fabricated LM–MMT composite ink. Scale bar: 10 μm. (e) Electrical conductivity of LM–MMT inks as a function of MMT content. Error bars indicate standard deviation, *n* = 3 per group. (f) Optical (scale bar: 2 mm) and SEM (scale bar: 10 μm) images of LM–MMT inks with varying MMT weight fractions. (g) Storage modulus (*G*′) and loss modulus (*G*″) as functions of angular frequency. (h) Stress–strain curves of LM–MMT inks at 1 rad s^{-1} shear rate. (i) Viscosity profiles of LM–MMT inks as functions of shear rate.

comprises irregular sub-10 μm flakes primarily containing silicon, oxygen, aluminum, and magnesium (Fig. 2b and Fig. S1).

Upon air exposure, gallium spontaneously forms a nanometric gallium oxide (Ga_2O_3) shell (∼6 nm) at the LM surface.[47–49] During mixing, this oxide gradually adheres to the MMT surface (Fig. 2c-i and ii). As the process continues, the original oxide is gradually depleted, allowing MMT particles to be uniformly dispersed within the LM matrix, while new oxide continuously re-forms through ongoing oxygen exposure (Fig. 2c-iii and iv).

SEM and EDS analyses of the resulting LM–MMT ink (Fig. 2d and Fig. S2) revealed that the composite contains elements from both LM (Ga, In) and MMT (Si, O, Al, Mg). Importantly, the incorporation of MMT does not significantly disrupt the conductive network formed by the liquid metal, resulting only in a gradual decrease in conductivity (Fig. 2e). At an optimized MMT-to-LM mass ratio of 5%, the ink achieves a conductivity of 2.34×10^6 S m^{-1}, slightly lower than pristine LM (3.21×10^6 S m^{-1}),[50,51] but still surpasses several previously reported printable conductive inks.[52–55]

Meanwhile, increased MMT content elevates the ink's surface roughness and induces a gradual transition from liquid to semi-solid behavior (Fig. 2f). The rheological performance of LM–MMT inks was systematically characterized to assess their printability (Fig. 2g–i). Frequency sweep analysis indicated that the storage modulus (G') distinctly exceeds the loss modulus (G'') over the explored frequency range, reflecting a dominant solid-like, viscoelastic response that favors the retention of printed features (Fig. 2g). Both moduli exhibited noticeable decreases at higher angular frequencies, potentially due to microstructural rearrangements under stress. In the strain sweep test, the shear stress of the ink exhibited minimal change as the strain increased from 0.1% to 100%, indicating linear viscoelasticity and stable rheological behavior. This property is essential for ensuring reliable printing performance (Fig. 2h). Moreover, all ink formulations exhibited pronounced shear-thinning behavior, as demonstrated by flow sweep measurements: viscosity decreased sharply with increasing shear rate, supporting smooth extrusion through fine nozzles during DIW (Fig. 2i). Notably, increasing MMT content correspondingly increased ink viscosity, yet each composite maintained robust shear-thinning characteristics suitable for extrusion-based printing. Collectively, these results demonstrate that the LM–MMT ink formulation provides a favorable balance

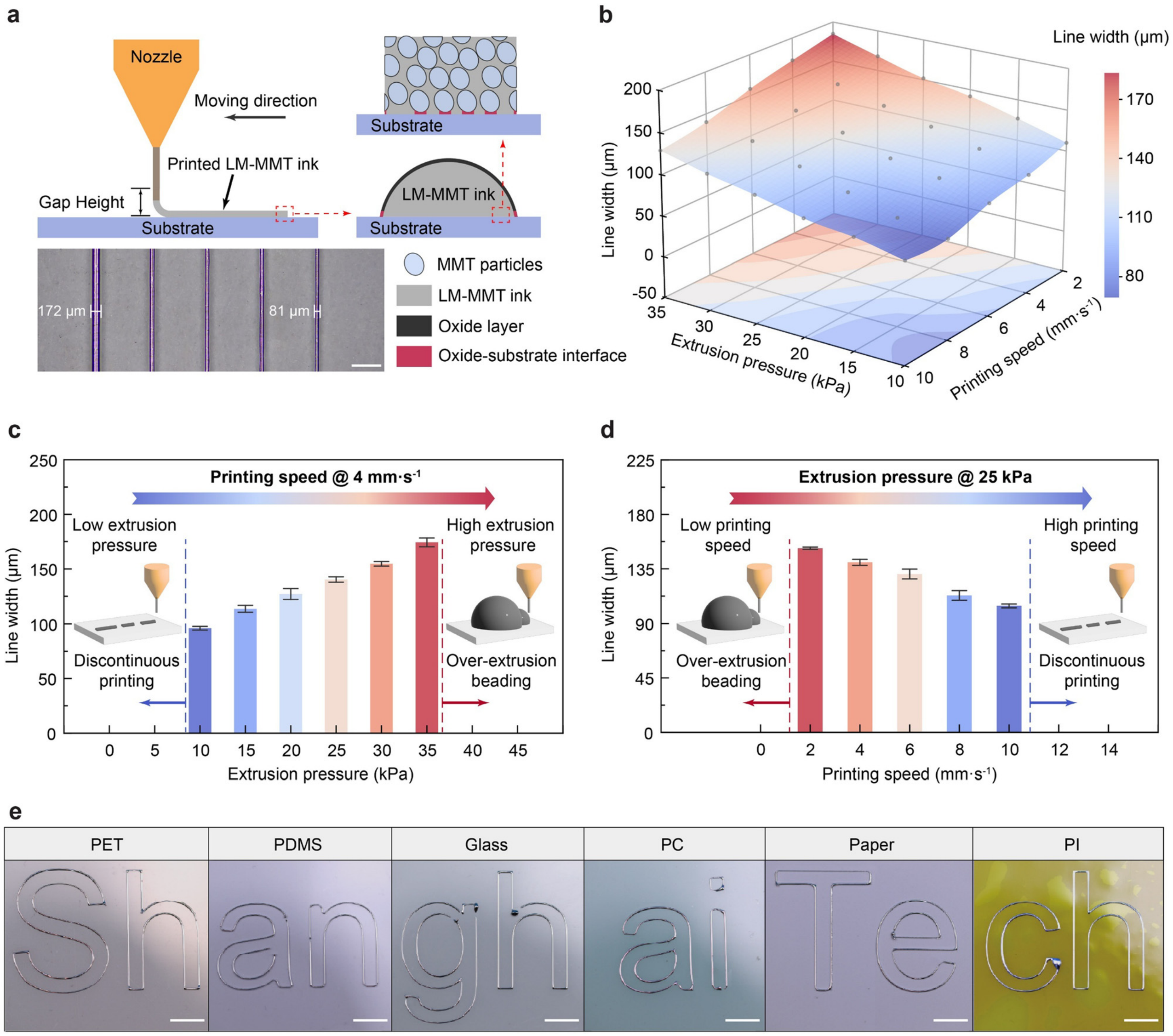

Fig. 3 Direct ink writing of LM–MMT ink. (a) Schematic of the DIW mechanism for LM–MMT ink, alongside an optical image of printed traces on a Ecoflex substrate. Scale bar: 500 μm. (b) Printed linewidth as a function of extrusion pressure and printing speed. (c) Linewidth variation as a function of extrusion pressure at a constant printing speed of 4 mm s^{-1}. Error bars denote standard deviation, n = 3 per group. (d) Linewidth variation as a function of print speed at a set extrusion pressure of 25 kPa. Error bars denote standard deviation, n = 3 per group. (e) Demonstration of complex patterning by printing the word "ShanghaiTech" with LM–MMT ink on various substrates, including PET, PDMS, glass, polycarbonate (PC), paper, and polyimide (PI). Scale bars: 10 mm.

between rheological performance and conductivity behavior, affording reliable patterning of high-resolution stretchable bioelectronics.

2.3. Direct ink writing of LM–MMT ink

The LM–MMT ink is amenable to direct ink writing *via* pneumatic extrusion, enabling high-resolution deposition onto a wide array of substrates. The operational workflow for DIW patterning is illustrated in Fig. 3a. The inclusion of MMT particles enhance the microstructural roughness of the ink surface, which effectively suppressing surface tension effects and enhancing substrate wettability through capillary action. Simultaneously, the MMT particles, coated with a gallium oxide shell, enhance interfacial adhesion to the substrate, thereby stabilizing the deposited traces (Fig. S3 and S4). SEM images reveal that the printed trace exhibits an arch-like profile (Fig. S5a). The strong interfacial bonding between the gallium oxide shell and the substrate, combined with the structural rigidity provided by the MMT particles, ensures reliable shape retention of the printed features (Fig. S5b).[56]

Prior to printing, the ink is loaded into a syringe and extruded through a standard dispensing needle. Precise control of the nozzle-to-substrate distance is critical: insufficient distance can obstruct flow, while excessive separation compromises printing accuracy. With 5 wt% LM–MMT ink delivered through a 23-gauge needle under optimized pressure-speed conditions, the resultant linewidth ranged from 81 μm to 172 μm (Fig. 3b). Through the use of higher-gauge needles, the minimal linewidth was further decreased to 70 μm. Notably, these values are substantially narrower than those reported for printable LM inks to date.[57–61] Printing tests revealed that the 5 wt% LM–MMT ink maintained its stability without any phase separation during extrusion (Fig. S6), whiles higher MMT content could result in increased printing pressure and phase separation.

Further analysis revealed that linewidth increases with extrusion pressure (10–35 kPa) at a fixed print speed of 4 mm s^{-1} (Fig. 3c). Pressures below 10 kPa result in intermittent line formation due to under-extrusion, while pressures exceeding 35 kPa cause over-extrusion and droplet formation, deteriorating pattern precision (Movie S3). Similarly, at a constant pressure of 25 kPa, increasing the print speed from 2 to 10 mm s^{-1} leads to a reduction in linewidth (Fig. 3d). Speeds below 2 mm s^{-1} result in excessive material deposition, whereas speeds above 10 mm s^{-1} produce discontinuous lines and reduced positional accuracy. Through careful optimization of print speed and extrusion pressure, target linewidths can be reproducibly achieved, enabling accurate fabrication of intricate conductive patterns. The LM–MMT ink demonstrates excellent compatibility with a wide range of substrates, including PET, PDMS, glass, polycarbonate (PC), paper, and polyimide (PI). Contact angle measurements across these substrates revealed that LM–MMT ink droplets consistently displayed reduced contact angles compared to pure liquid metal, with values decreasing systematically as MMT content increased (Fig. S7). This consistent reduction demonstrates that the incorporation of MMT significantly enhances the wettability of the ink on various substrates (Fig. S8). Collectively, these results highlight the strong potential of LM–MMT ink for diverse flexible and stretchable bioelectronic applications (Fig. 3e and Fig. S9).

2.4. Mechanical and electrical performance of LM–MMT device

We fabricated stretchable bioelectronic sensors by direct ink writing of LM–MMT ink onto elastomeric substrates. Ecoflex 00-30 was chosen as both the substrate and encapsulant due to its excellent flexibility and stretchability, making it well-suited for strain sensing. A straight conductive trace was printed onto cured Ecoflex 00-30, then encapsulated with a second layer of Ecoflex to yield a robust strain sensor. The strain sensor was subjected to controlled tensile testing with an initial gauge length of 3 cm and could be stretched up to 50% and even 100% strain without visible damage or loss of function (Fig. 4a). Relative resistance change ($\Delta R/R_0$) was obtain using an LCR meter and plotted as a function of applied strain (Fig. 4b). The gauge factor (GF), calculated from the resistance-strain relationship, demonstrates quasi-linear behaviour across all strain ranges, which ensures reliable deformation monitoring. We further integrated the printed conductive traces with LEDs, which maintained stable illumination under bending, stretching, and twisting conditions (Fig. S10 and S11). These results corroborate that the printed LM–MMT traces exhibit excellent electrical conductivity and mechanical robustness, confirming their suitability for the fabrication of complex-patterned bioelectronic devices.

Hysteresis characterization under cyclic loading and unloading (Fig. 4c) demonstrated that the sensor exhibited a low hysteresis ratio of 1.03 at 100% strain, confirming minimal energy loss and excellent accuracy during repeated operation. Resistance responses under various strain increments (Fig. 4d and e) were highly consistent, clearly distinguishing 10% changes in strain and confirming the device's high sensitivity. Frequency response testing (Fig. 4f) showed steady resistance profiles under different stretching rates, indicating reliable performance over a broad range of dynamic conditions.

Thermal stability was further evaluated by exposing the sensor to temperatures ranging from 25 °C to 95 °C (Fig. 4g). The sensor exhibited only a 6.65% increase in resistance across this range, confirming stable operation under both ambient and elevated temperature conditions. Notably, the sensor exhibited exceptional durability; after 2500 consecutive stretching cycles at 50% strain, its resistance response remained remarkably stable (Fig. 4h). Detailed comparison of the initial, middle, and final cycles further confirmed outstanding signal repeatability and durability. Collectively, these mechanical and electrical performance results strongly support the viability of LM–MMT-based devices for bioelectronic sensing applications.

2.5. Application of LM–MMT device for human–machine interaction

The LM–MMT strain sensors, encapsulated in Ecoflex 00-30, exhibit outstanding stretchability and fatigue resistance, making them well-suited for capturing a wide range of

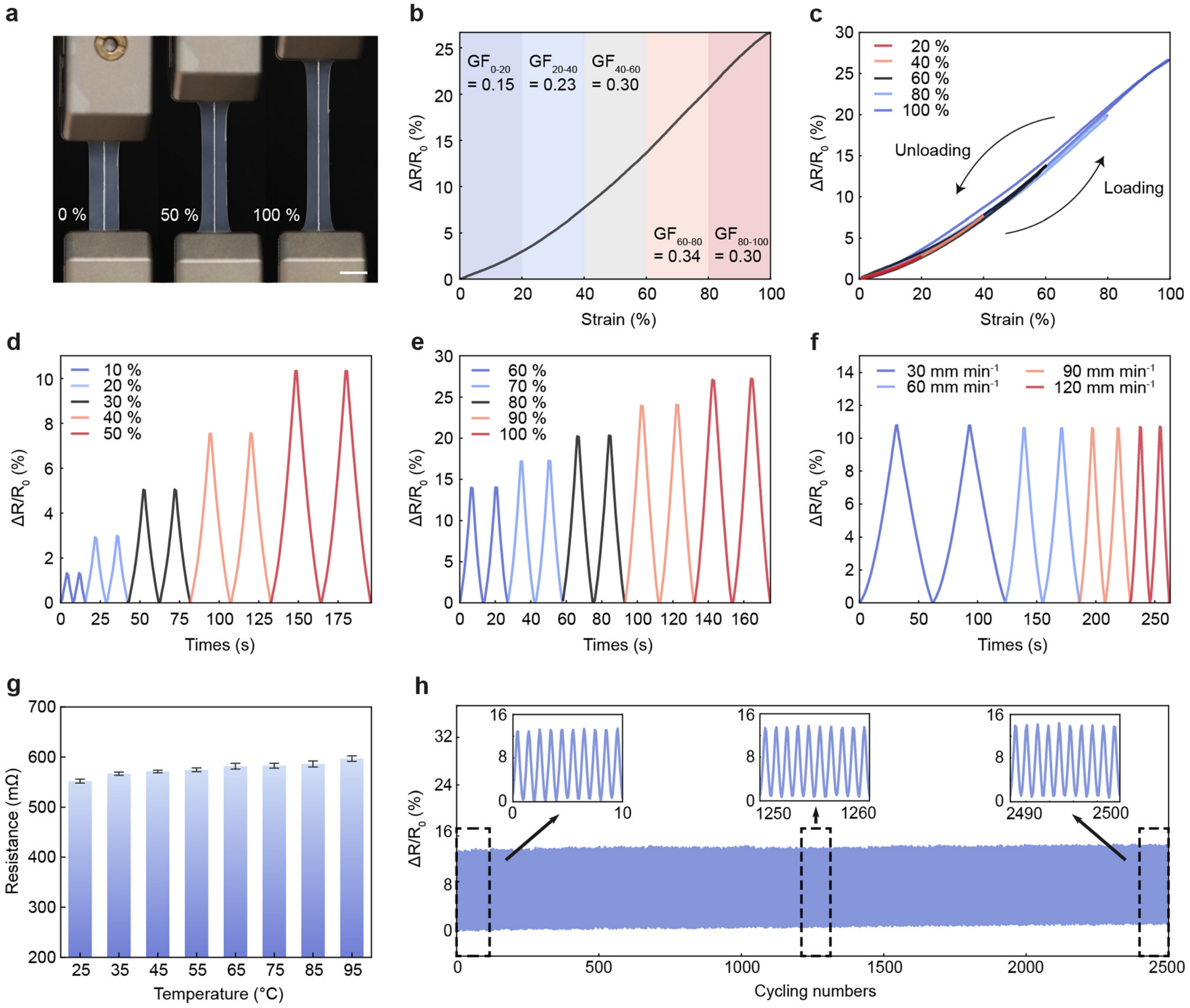

Fig. 4 Mechanical and electrical performance of LM–MMT strain sensor. (a) Optical images of the strain sensor under 0%, 50%, and 100% tensile strain. Scale bar: 10 mm. (b) Relative resistance of the sensor as a function of applied strain. (c) Hysteresis behavior showing resistance response during cyclic loading and unloading at various strain levels. (d) and (e) Relative resistance change of the strain sensor under different elongation ratios. (f) Relative resistance change of the strain sensor under different stretching rates. (g) Resistance variation of the strain sensor as a function of temperature. Error bars denote standard deviation, *n* = 3 per group. (h) Resistance change of the strain sensor over 2500 consecutive stretching cycles at 50% strain.

biomechanical motions. Owing to their mechanical modulus—closely matching that of human skin—these sensors demonstrate excellent conformability and adhesion to various body regions, particularly dynamic joint areas such as the fingers, wrist, elbow, knee, and neck. During joint movement, the sensor experiences elongation or contraction corresponding to the joint's bending angle, resulting in readily detectable resistance changes. When affixed to a finger joint and the finger is bent at discrete angles (0°, 30°, 45°, 60°, 90°), $\Delta R/R_0$ increases proportionally from 0% to 20.4% (Fig. 5a). The resulting resistance profiles allow for clear differentiation among finger positions, enabling accurate gesture recognition.

The applicability of the sensor extends to additional joints, as demonstrated by its performance in real-time motion tracking of the wrist, elbow, and knee (Fig. 5b–d). When attached to the skin surface, the sensor stretches and elongates during joint flexion (Fig. S12). Specifically, a 90° wrist flexion results in a $\Delta R/R_0$ increase from 0% to 24.7%. Similarly, flexion of the elbow and knee by approximately 90° yields relative resistance changes of 60.8% and 32.7%, respectively. Placement on the neck further enables detection of subtle strain variations associated with physiological activities. For example, rapid vertical movement of the laryngeal prominence during swallowing produces a transient resistance change from −1.7% to 1.3% (Fig. 5e), while head rotation induces distinct stretch or compression patterns, resulting in characteristic resistance changes up to 5.7% (Fig. 5f).

To demonstrate system-level scalability and integration, multiple LM–MMT strain sensors were fabricated and mounted on different finger joints for multi-channel signal acquisition.

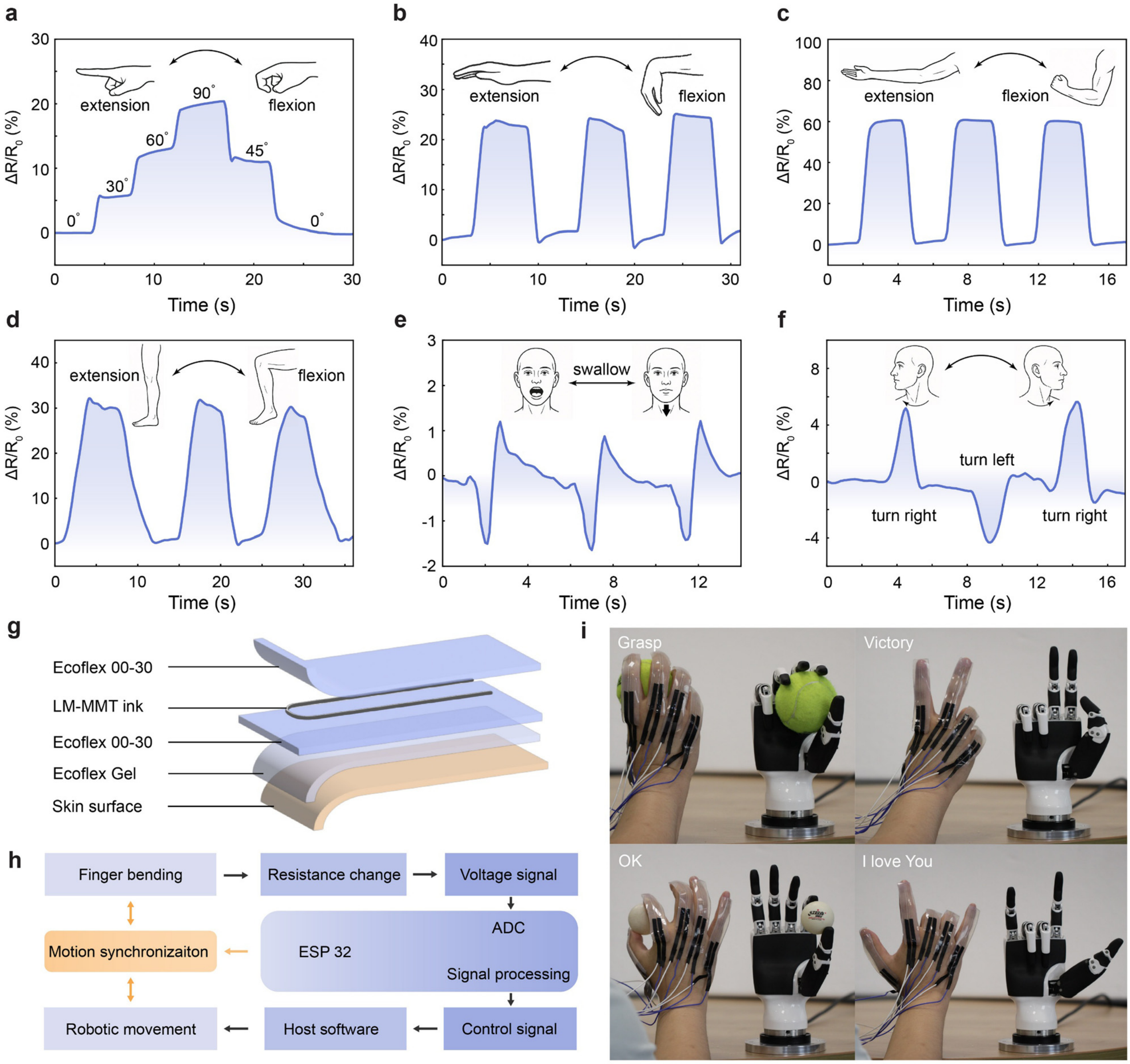

Fig. 5 LM–MMT sensors for human motion monitoring and human–machine interaction. (a) Relative resistance change of the sensor corresponding to different finger bending angles. (b) Relative resistance change of the sensor during wrist flexion and extension. (c) Relative resistance change of the sensor during elbow movement. (d) Relative resistance change of the sensor during knee bending and straightening. (e) Relative resistance change of the sensor during swallowing. (f) Relative resistance change of the sensor during head rotation to the left and right. (g) System flowchart illustrating real-time robotic control enabled by LM–MMT sensor. (h) System flowchart for human–machine interaction based on hand motion sensing. (i) Demonstration of a robotic hand controlled in real time by human hand movements.

The configuration of the strain sensor is depicted in Fig. 5g. Real-time figure motion signal was acquired by an ESP32-based readout circuit and transferred to a robotic dexterous hand, enabling gesture recognition and reproduction (Fig. 5h). In this setup, each sensor serves as a variable resistor within a voltage divider circuit, and its output is continuously sampled by the ESP32's analog-to-digital converter (Fig. S13 and Table S2). The digitized signals are processed and relayed to controlling computer, facilitating seamless translation of human hand gestures into corresponding robotic movements (Movie S4). A series of complex human hand gestures were replicated by robotic hand—such as grasping, "Victory," "OK," and "I love you"—as shown in Fig. 5i. These results underscore the precise, and responsive nature of LM–MMT bioelectronic sensors, positioning them as promising candidates for wearable sensing, continuous health monitoring and advanced human–machine interface applications.

3. Conclusion

In summary, we have developed a printable liquid metal–montmorillonite (LM–MMT) composite ink by mechanically blending gallium-based liquid metal with naturally abundant, inexpensive MMT powder. During the mixing process, the gradual encapsulation of MMT particles with gallium oxide promotes dynamic oxide layer consumption and regeneration, ultimately enhancing the ink's adhesion to a diverse range of substrates. Importantly, the incorporation of MMT particles does not compromise the continuous conductive pathways of the liquid metal, thereby preserving excellent electrical conductivity without external activation. This unique combination of high printability and robust conductivity renders the LM–MMT ink highly attractive for the fabrication of flexible and stretchable bioelectronic devices.

Direct ink writing of the LM–MMT ink enables the fabrication of strain sensors that exhibit remarkable mechanical reliability, low hysteresis, and high sensitivity across large deformation ranges. These sensors not only capture gross human joint movements but also effectively detect subtle physiological signals, such as swallowing and neck rotation. Moreover, the integration of multi-channel LM–MMT sensors facilitates real-time gesture recognition and remote robotic control, establishing a seamless and responsive human–machine interface.

Overall, the LM–MMT ink represents a scalable and cost-effective platform for high-resolution patterning of stretchable bioelectronic devices. Its demonstrated performance in wearable sensing, health monitoring, and interactive systems underscores its significant potential for next-generation bioelectronic applications.

4. Experimental section

4.1. Materials

Eutectic gallium–indium alloy (EGaIn, Ga : In = 75.5 : 24.5, melting point: 16 °C) was used as the liquid metal (LM) and sourced from Dingguan Metal Technology Co., Ltd. Montmorillonite (MMT) powder (99%, particle size: 3000 mesh) was obtained from Dongxin Biotechnology Co., Ltd. Ecoflex 00-30 and Ecoflex Gel (Smooth-On, Inc.) were prepared by mixing parts A and B in a 1 : 1 weight ratio. Polydimethylsiloxane (PDMS; Sylgard 184, Dow Corning) was prepared by mixing the base and curing agent at a 10 : 1 weight ratio. Surface-mount LEDs (0805) were supplied by LCSC Electronics Co., Ltd. Polyvinyl chloride (PVC) substrates were purchased from Changhe Plastics Co., Ltd. Polyimide (PI), polyethylene terephthalate (PET), and polycarbonate (PC) substrates were sourced from Ruyuan Plastics Co., Ltd. Glass substrates were obtained from Ningmeng Laboratory Equipment Co., Ltd.

4.2. Preparation of LM–MMT ink

MMT was added to the liquid metal at mass ratios of 2.5%, 5%, 7.5%, and 10%. The mixtures were processed using a planetary centrifugal mixer (BHJ-3, BHLAB) at room temperature. Initially, the mixture was stirred at 200 rpm for 5 minutes, followed by 1000 rpm for 30 minutes. After mixing, a homogeneous LM–MMT ink was obtained. Prior to each use, the ink was degassed and rehomogenized at 200 rpm for 5 minutes using the same mixer to remove air bubbles and ensure uniformity.

4.3. Fabrication of LM–MMT strain sensor

The LM–MMT ink was patterned using a direct ink writing (DIW) system consisting of a 3-axis motion platform (AUS-PRECISION) controlled *via* SPiiPlusSPC software (ACS Motion Control). The ink was loaded into a syringe and extruded through a 23-gauge needle (inner diameter: 300 μm) using a pneumatic regulator, with the extrusion pressure set to 25 kPa and the printing speed maintained at 4 mm s^{-1}. Sensor patterns were designed in AutoCAD (Autodesk).

For device fabrication, Ecoflex parts A and B were mixed at a 1 : 1 ratio and cast into a Petri dish, then cured at room temperature for 4 hours to form a flexible substrate. LM–MMT ink was printed onto the cured Ecoflex substrate, followed by encapsulation with an additional layer of Ecoflex mixture, and cured again at room temperature for 4 hours. The resulting sensor had a typical thickness of approximately 2 mm. For wearable applications, an additional layer of Ecoflex Gel (A : B = 1 : 1) was cast on the top surface to enhance skin adhesion.

4.5. Characterization

Photographs were captured using a digital camera (EOS 60D, Canon). Sample morphology and elemental composition were characterized *via* scanning electron microscopy equipped with energy-dispersive X-ray spectroscopy (SEM, JSM-7800F, JEOL) at an acceleration voltage of 10 kV. Printed linewidths under various parameters were measured with a digital microscope (H2607T, OSEECAM).

Rheological properties of the LM–MMT ink were measured at 25 °C using a rotational rheometer (HAAKE MARS iQ AIR, Thermo Fisher Scientific). The gap between the stainless-steel plates was set to 1 mm. Samples were pre-sheared at a rate of 1 s^{-1} for 120 seconds before testing. Frequency sweeps were conducted at 0.5% strain in the range of 0.1–100 rad s^{-1} to obtain storage modulus (G') and loss modulus (G''). Strain sweeps were performed at a fixed angular frequency of 1 rad s^{-1} with strain amplitudes ranging from 0.1% to 100%. Flow sweeps from 0.001 to 10 s^{-1} were used to characterize the viscosity–shear rate relationship.

Electrical performance was evaluated by simultaneously recording resistance using an LCR meter (PXIe-4190, National Instruments) during mechanical testing with a tensile testing machine (F105, MARK-10).

The relative resistance change of the strain sensors was calculated using:

$$\frac{\Delta R}{R_0} = \frac{(R - R_0)}{R_0} \times 100\%$$

where R_0 is the initial resistance and R is the resistance under applied strain. The gauge factor (GF), which quantifies strain sensitivity, was defined as:

$$\mathrm{GF} = \left(\frac{\Delta R}{R_0}\right)/\varepsilon$$

where ε is the applied strain.

Hysteresis (γ_H) was calculated using the following equation:

$$\gamma_H = \frac{|\Delta R|_{\max}}{\Delta R_{\text{full}}} = \frac{|\Delta R_{\text{load}} - \Delta R_{\text{unload}}|_{\max}}{\Delta R_{\text{full}}}$$

where ΔR_{load} and ΔR_{unload} are the resistance changes during loading (stretching) and unloading (releasing), respectively; $|\Delta R|_{\max}$ is the maximum difference in resistance between the loading and unloading paths at the same strain level; and ΔR_{full} is the total resistance change over the full strain range (from 0 to maximum strain).

For conductivity measurements, a custom groove mold (20 mm × 1 mm × 1 mm) was fabricated using a 3D printer (A1 mini, Bambu Lab). LM–MMT ink was filled into the groove and the surface was leveled. Electrical resistance (R) was measured using a benchtop digital multimeter (SDM3055X-E, SIGLENT) with the four-point probe method. The electrical conductivity (σ) was calculated as:

$$\sigma = \frac{L}{R \cdot A}$$

where L is the length and A is the cross-sectional area of the conductive path. All measurements were averaged over at least three independently prepared samples, and standard deviations were reported.

Informed consent was obtained from all participants prior to their involvement in the human–machine interaction experiments.

Author contributions

Ziang Cui: conceptualization, validation, investigation, methodology, data curation, visualization, writing – original draft. Yiqing Zhang and Siyuan Chen: investigation, data analysis. Xingming Wen, Yitao Ma, Qihang Yan, Zixiong Wu, and Yuxi He: investigation. Yining Zhao: software. Guohui Wang, Ziyuan Tang, Chenxi Xiao, and You Yu: methodology, resources. Jianrui Li: funding acquisition, data analysis, writing – review & editing. Ze Xiong: conceptualization, project administration, funding acquisition, supervision, writing – review & editing.

Conflicts of interest

There are no conflicts to declare.

Data availability

The data supporting this article have been included as part of the SI. Supplementary information available: SEM and EDS characterizations, adhesion force evaluation, contact angle measurements, printability and conductivity characterizations, and circuit design. See DOI: https://doi.org/10.1039/d5tc02256h

Acknowledgements

Ze Xiong acknowledges the support from the Science and Technology Commission of Shanghai Municipality (24490710900) and the start-up grant from ShanghaiTech University (2023F0209-000-02). Jianrui Li acknowledges the support from China University Research Innovation Fund – Digital Health Project (2023GY056). You Yu acknowledges the support from National Natural Science Foundation of China (22304117) and CIE-Tencent Robotics X Rhino-Bird Focused Research Program.

References

1 A. F. Wibowo, J. W. Han, J. H. Kim, A. Prameswati, S. A. N. Entifar, J. Park, J. Lee, S. Kim, D. C. Lim, Y. Eom, M.-W. Moon, M.-S. Kim and Y. H. Kim, *ACS Appl. Mater. Interfaces*, 2023, **15**, 18134–18143.

2 C. Sun, Z. Han, X. Wang, B. Liu, Q. Li, H. Li, J. Xu, J.-M. Cao and X.-L. Wu, *Adv. Funct. Mater.*, 2023, **33**, 2305606.

3 T. Li, Y. Li and T. Zhang, *Acc. Chem. Res.*, 2019, **52**, 288–296.

4 C. S. Xu, D. F. Jiang, Y. C. Ge, L. P. Huang, Y. Xiao, X. Q. Ren, X. H. Liu, Q. W. Zhang and Y. Wang, *Chem. Eng. J.*, 2022, **431**, 134109.

5 S. P. Lacour, G. Courtine and J. Guck, *Nat. Rev. Mater.*, 2016, **1**, 16063.

6 K. Sugioka and Y. Cheng, *Lab Chip*, 2012, **12**, 3576–3589.

7 H. Chang, S. Kim, S. Jin, S. W. Lee, G. T. Yang, K. Y. Lee and H. Yi, *ACS Appl. Mater. Interfaces*, 2018, **10**, 1067–1076.

8 J. N. Koster, *Cryst. Res. Technol.*, 1999, **34**, 1129–1140.

9 Y. G. Park, H. S. An, J. Y. Kim and J. U. Park, *Sci. Adv.*, 2019, **5**, eaaw2844.

10 B. Feng, X. Jiang, G. S. Zou, W. G. Wang, T. M. Sun, H. Yang, G. L. Zhao, M. Y. Dong, Y. Xiao, H. W. Zhu and L. Liu, *Adv. Funct. Mater.*, 2021, **31**, 2102359.

11 S. X. Xiang, D. J. Liu, C. C. Jiang, W. M. Zhou, D. Ling, W. T. Zheng, X. P. Sun, X. Li, Y. C. Mao and C. X. Shan, *Adv. Funct. Mater.*, 2021, **31**, 2100940.

12 P. C. Wu, Z. W. Wang, X. H. Yao, J. Z. Fu and Y. He, *Mater. Horiz.*, 2021, **8**, 2006–2017.

13 N. Lazarus, S. S. Bedair and I. M. Kierzewski, *ACS Appl. Mater. Interfaces*, 2017, **9**, 1178–1182.

14 R. Guo, X. Wang, H. Chang, W. Yu, S. Liang, W. Rao and J. Liu, *Adv. Eng. Mater.*, 2018, **20**, 1800054.

15 M. Varga, C. Ladd, S. Y. Ma, J. Holbery and G. Tröster, *Lab Chip*, 2017, **17**, 3272–3278.

16 H. Chang, R. Guo, Z. Sun, H. Wang, Y. Hou, Q. Wang, W. Rao and J. Liu, *Adv. Mater. Interfaces*, 2018, **5**, 1800571.

17 T. V. Neumann and M. D. Dickey, *Adv. Mater. Technol.*, 2020, **5**, 2000070.

18 Z. Zou, Y. Chen, S. Yuan, N. Luo, J. Li and Y. He, *Adv. Funct. Mater.*, 2023, **33**, 2213312.

19 A. Haake, R. Tutika, G. M. Schloer, M. D. Bartlett and E. J. Markvicka, *Adv. Mater.*, 2022, **34**, 2200182.

20 S. Pak, M. D. Bartlett and E. J. Markvicka, *Adv. Funct. Mater.*, 2024, **34**, 2410908.

21 C. Wang, Y. Gong, B. V. Cunning, S. Lee, Q. Le, S. R. Joshi, O. Buyukcakir, H. Zhang, W. K. Seong, M. Huang, M. Wang, J. Lee, G.-H. Kim and R. S. Ruoff, *Sci. Adv.*, 2021, **7**, eabe3767.

22 X. Zhao, S. Xu and J. Liu, *Front. Energy*, 2017, **11**, 535–567.

23 J. Tang, X. Zhao, J. Li, R. Guo, Y. Zhou and J. Liu, *ACS Appl. Mater. Interfaces*, 2017, **9**, 35977–35987.

24 I. D. Joshipura, H. R. Ayers, G. A. Castillo, C. Ladd, C. E. Tabor, J. J. Adams and M. D. Dickey, *ACS Appl. Mater. Interfaces*, 2018, **10**, 44686–44695.

25 L. Tang, J. Shang and X. Jiang, *Sci. Adv.*, 2021, **7**, eabe3778.

26 D. Xu, J. Cao, F. Zhang, X. Gao, S. Li, F. Liu, S. Wang, S. Li, J. Liu, Y. Wu, Y. Liu, J. Shang and R.-W. Li, *Mater. Today Phys.*, 2023, **38**, 101239.

27 M. D. Bartlett, M. D. Dickey and C. Majidi, *NPG Asia Mater.*, 2019, **11**, 21.

28 S. Liu, Z. Xu, G. Li, Z. Li, Z. Ye, Z. Xu, W. Chen, D. Jin and X. Ma, *Adv. Sci.*, 2023, **10**, 2301292.

29 R. Guo, X. Sun, B. Yuan, H. Wang and J. Liu, *Adv. Sci.*, 2019, **6**, 1901478.

30 B. Ma, C. Xu, J. Chi, J. Chen, C. Zhao and H. Liu, *Adv. Funct. Mater.*, 2019, **29**, 1901370.

31 Y. Li, S. Feng, S. Cao, J. Zhang and D. Kong, *ACS Appl. Mater. Interfaces*, 2020, **12**, 50852–50859.

32 D. A. Kwon, S. Lee, C. Y. Kim, I. Kang, S. Park and J.-W. Jeong, *Sci. Adv.*, 2024, **10**, eadn1186.

33 M. R. Carneiro, C. Majidi and M. Tavakoli, *Adv. Eng. Mater.*, 2022, **24**, 2100953.

34 S. J. Cho, G. D. Kong, S. Park, J. Park, S. E. Byeon, T. Kim and H. J. Yoon, *Nano Lett.*, 2019, **19**, 545–553.

35 R. Guo, X. Sun, S. Yao, M. Duan, H. Wang, J. Liu and Z. Deng, *Adv. Mater. Technol.*, 2019, **4**, 1900183.

36 R. Guo, H. Wang, X. Sun, S. Yao, H. Chang, H. Wang, J. Liu and Y. Zhang, *ACS Appl. Mater. Interfaces*, 2019, **11**, 30019–30027.

37 M. J. Ford, D. K. Patel, C. Pan, S. Bergbreiter and C. Majidi, *Adv. Mater.*, 2020, **32**, 2002929.

38 J. Xu, H. Guo, H. Ding, Q. Wang, Z. Tang, Z. Li and G. Sun, *ACS Appl. Mater. Interfaces*, 2021, **13**, 7443–7452.

39 S. Moon, H. Kim, K. Lee, J. Park, Y. Kim and S. Q. Choi, *iScience*, 2021, **24**, 103183.

40 L.-y Zhou, J.-z Fu, Q. Gao, P. Zhao and Y. He, *Adv. Funct. Mater.*, 2020, **30**, 1906683.

41 M. Reis Carneiro, C. Majidi and M. Tavakoli, *Adv. Funct. Mater.*, 2022, **32**, 2205956.

42 L. Tang, J. Shang and X. Jiang, *Sci. Adv.*, 2021, **7**, eabe3778.

43 P. Wu, J. Fu, Y. Xu and Y. He, *ACS Appl. Mater. Interfaces*, 2022, **14**, 13458–13467.

44 E. J. Markvicka, M. D. Bartlett, X. Huang and C. Majidi, *Nat. Mater.*, 2018, **17**, 618–624.

45 G. Gao, G. Du, Y. Sun and J. Fu, *ACS Appl. Mater. Interfaces*, 2015, **7**, 5029–5037.

46 W. Chen, Y. Hu, W. Lv, T. Lei, X. Wang, Z. Li, M. Zhang, J. Huang, X. Du, Y. Yan, W. He, C. Liu, M. Liao, W. Zhang, J. Xiong and C. Yan, *Nat. Commun.*, 2019, **10**, 4973.

47 Z. J. Farrell and C. Tabor, *Langmuir*, 2018, **34**, 234–240.

48 M. J. Regan, H. Tostmann, P. S. Pershan, O. M. Magnussen, E. DiMasi, B. M. Ocko and M. Deutsch, *Phys. Rev. B*, 1997, **55**, 10786–10790.

49 M. K. Akbari, F. Verpoort and S. Zhuiykov, *J. Mater. Chem. A*, 2021, **9**, 34–73.

50 R. C. Chiechi, E. A. Weiss, M. D. Dickey and G. M. Whitesides, *Angew. Chem. Int. Ed.*, 2008, **47**, 142–144.

51 M. D. Dickey, *Adv. Mater.*, 2017, **29**, 1606425.

52 Z. Song, J. Ma, R. Fang, J. Liu and H. Wang, *ACS Appl. Electron. Mater.*, 2024, **6**, 3884–3893.

53 L. Zhu, X. Zhou, J. Zhang, Y. Xia, M. Wu, Y. Zhang, Z. Lu, W. Li, L. Liu, H. Liu, J. Yu and J. Xiong, *ACS Nano*, 2024, **18**, 34750–34762.

54 X. Li, M. Li, L. Zong, X. Wu, J. You, P. Du and C. Li, *Adv. Funct. Mater.*, 2018, **28**, 1804197.

55 G.-H. Lee, Y. R. Lee, H. Kim, D. A. Kwon, H. Kim, C. Yang, S. Q. Choi, S. Park, J.-W. Jeong and S. Park, *Nat. Commun.*, 2022, **13**, 2643.

56 G. Li, M. Parmar and D. W. Lee, *Lab Chip*, 2015, **15**, 766–775.

57 W. Chen, Q. Tang, W. Zhong, M. Lai, S. Shi, J. Tan, Z. Luo, X. Liu, Z. Ye, R. He, F. Jiang, X. Zhou and B. Wang, *Adv. Funct. Mater.*, 2025, **35**, 2411647.

58 D. P. Parekh, C. M. Fancher, M. G. Mohammed, T. V. Neumann, D. Saini, J. Guerrier, C. Ladd, E. Hubbard, J. L. Jones and M. D. Dickey, *ACS Appl. Nano Mater.*, 2020, **3**, 12064–12070.

59 J. W. Boley, E. L. White, G. T. C. Chiu and R. K. Kramer, *Adv. Funct. Mater.*, 2014, **24**, 3501–3507.

60 C. Ladd, J. H. So, J. Muth and M. D. Dickey, *Adv. Mater.*, 2013, **25**, 5081–5085.

61 A. Tabatabai, A. Fassler, C. Usiak and C. Majidi, *Langmuir*, 2013, **29**, 6194–6200.